ELSEVIER

Contents lists available at ScienceDirect

Journal of Power Sources

journal homepage: www.elsevier.com/locate/jpowsour





Understanding thermal and mechanical effects on lithium plating in lithium-ion batteries

Yitao Qiu^a, Xiaoxuan Zhang^b, Camille Usubelli ^{c,d}, Daniel Mayer^c, Christian Linder ^{a,e}, Jake Christensen ^{c,*}

- a Department of Civil and Environmental Engineering, Stanford University, Stanford, CA, 94305, USA
- ^b Department of Mechanical Engineering, University of Michigan, Ann Arbor, MI, 48109, USA
- c Robert Bosch LLC, Research and Technology Center, Sunnyvale, CA, 94085, USA
- d Institute of Physics and Chemistry of Materials of Strasbourg, UMR 7504 CNRS, University of Strasbourg, F-67034 Strasbourg Cedex 2, France
- e Department of Mechanical Engineering, Stanford University, Stanford, CA, 94305, USA

HIGHLIGHTS

- · 1D and 3D Li-ion cell models explore the impact of mechanics on lithium plating.
- · Lower temperature increases the risk of lithium plating.
- · Mechanical deformation can accelerate the initiation of lithium plating.
- · Folds and boundaries of jellyrolls are more vulnerable to lithium plating.
- · Implications for fast charging algorithms are explored.

ARTICLE INFO

Keywords: Lithium-ion battery DualFoil model Lithium plating Thermal effects Mechanical effects

ABSTRACT

Lithium plating is one of the main concerns for cell durability, as cyclable lithium and cell capacity are decreased during the process. Thermal and mechanical loads can influence cell behavior, including lithium plating driving forces, as suggested by the Arrhenius equation and the Bruggeman relation, respectively. Hence, a 1D and a 3D model are employed to study the thermal and mechanical effects on lithium plating in a lithium-ion battery with a high areal capacity (4 mAh/cm²). The 1D model assumes uniform mechanical and temperature profile, while the 3D model is capable of capturing the nonuniformity of stress and temperature in the cell. The effects of mechanical deformation and different temperatures on the process of lithium plating are investigated in this study. With the help of the 1D charging simulations, it is observed that lower temperatures increase the risk of lithium plating and the presence of mechanical deformations can accelerate its initiation. Furthermore, 3D charging simulations indicated that folds and boundaries of jellyrolls are more susceptible to lithium plating due to the higher stress concentration and lower temperature, respectively.

1. Introduction

Lithium-ion batteries are widely used in various electronic devices such as cell phones, laptops, tablets, wireless headphones, and other electronic applications. Recently, a growing demand for batteries with extended cycle and calendar life, in addition to increased energy density, is driven by the rapid development of electric vehicles. Due to their importance, there have been many studies in the recent past that have investigated the effects of factors like material properties, cell designs, manufacturing processes, operating conditions and management strategies on the durability of lithium-ion batteries [1–5]. Lithium plating is

one such phenomenon which has been found to be one of the main concerns for the aging of lithium-ion batteries [6,7].

Lithium plating refers to the formation of metallic lithium on the anode surface leading to capacity loss, as the process consumes cyclable lithium [8–10]. This undesired reaction is thermodynamically favorable when the local anode surface overpotential drops below 0 V, which is usually seen at lower temperatures or due to fast charging [11–14]. Continual growth of uneven lithium plating, usually in the form of dendrites or mosses, can further penetrate the separator and induce internal short circuit [15–17]. In addition, the reaction between the

E-mail address: jake.christensen@us.bosch.com (J. Christensen).

Corresponding author.

deposited lithium and the electrolyte solvent at high temperatures can accelerate the thermal runaway of lithium-ion batteries, even resulting in fire and explosions [18,19].

It has been found that lithium plating is more favored at lower temperatures. According to the Arrhenius equation [20], lower temperatures decrease the ionic conductivity in the electrolyte, slow down the diffusion of lithium ions in both the electrolyte and the anode active material, and reduce the charge transfer rate on the anode surface [21, 22]. As lithium ions accumulate at the interface between the anode and the electrolyte due to poor transport, the surface concentration in the active material particles tends toward its maximum [22-24]. This in turn drives the lithium plating surface overpotential below zero, leading to lithium plating. Waldmann et al. [25] reconstructed commercial 16Ah lithium-ion cells for the purpose of anode surface overpotential measurements, and the effects of low diffusivity on lithium plating was demonstrated. Poor electrolyte transport at low temperature exacerbates the issue by concentrating the lithium insertion current near the anode/separator interface, effectively imparting a higher local C rate to the active material particles.

Similarly, volume expansion of the anode active material can reduce the effective electrolyte transport properties, via the Bruggeman relation, by reducing the electrolyte porosity. However, unlike with thermal effects, there has been a scarcity of both experimental and numerical modeling studies in the literature that focus on exploring the mechanical effects on lithium plating in lithium-ion batteries. Among the few existing studies, Cannarella and Arnold [26] investigated the effects of mechanical stress on the capacity of constrained lithiumion cells. In their experiments, cells subject to high stack pressure (initially 5 MPa and then varying between 1 MPa and 3 MPa) exhibit the highest rate of capacity degradation, while cells with low stack pressure (initially 0.05 MPa and then varying between 0 and 0.5 MPa) exhibit the lowest rate, even better than unconstrained ones. The authors further observed a large area of vertically aligned films in some specific locations of the anode with similar mechanical environment, and established a link between lithium plating and mechanics [27]. Both experiments and simulations show that local defects created or aggravated by mechanical stress can cause electrochemical instability leading to lithium plating. Birkenmaier et al. [28] reported that lithium plating in cells tends to start from a thin line near the cell edge, which could be a result of the unique mechanical environment on the boundary.

As the mechanical effects on lithium plating is not well observed in experiments in the past, previous modeling work mostly focuses on thermal effects. Based on the model described by Christensen et al. [29], Kim et al. [30] studied the thermal effects on lithium plating in 50-Ah automotive cells. The authors demonstrated that lithium plating is more likely to occur around the exterior of the jellyroll due to its lower temperature, and more lithium plating is expected at lower ambient temperatures. However, the authors only considered thermal effects in their simulations, without accounting for the effects of mechanical deformation. Recently, Zhang et al. [31] proposed a 1D modified electrochemical model to describe the mechanical effects sourced from external applied pressure and lithium intercalation/deintercalation. Further, a 3D multiphysics model was developed by Zhang et al., by coupling the 1D modified electrochemical model with a 3D thermomechanical model based on finite strain theory. Although there are many models simulating thermal effects, very few models consider the amalgamation of thermal and mechanical effects on lithium plating.

This work investigates thermal and mechanical effects on lithium plating in lithium-ion batteries, based on Zhang et al.'s framework. The DualFoil model is a 1D physics-based model of a lithium-ion cell, encompassing concentrated solution theory, porous electrode theory, Ohm's law, Butler–Volmer kinetics, and current and mass conservation [33–35]. The 1D modified DualFoil model used in this work also accounts for the mechanical effects due to lithium intercalation and

external pressure by updating the porosity. The 3D multiphysics model couples the 1D modified DualFoil model with a 3D thermomechanical model through a spatial based mapping of independently resolved model meshes for the sake of efficiency [29]. The whole cell is divided into multiple sub-cells with identical voltage, and with currents summing to the specified total applied current. Thermal and mechanical effects on lithium plating are studied using these two models.

2. Methods

Numerically modeling the cell behavior is a challenging task due to the presence of the coupling of electric, chemical, thermal and mechanical effects. It has been shown in many studies that each component contributes significantly to the overall behavior. Among the existing models, the 1D modified DualFoil model assumes uniform stress and temperature, and simulates the cell behavior with mechanical deformation, while the 3D electro-chemo-thermo-mechanical model additionally captures the non-uniformity of stress and temperature in cells. In the upcoming subsections, the 1D modified DualFoil model and the 3D electro-chemo-thermo-mechanical model are described. In addition, we also introduce the model parameterization for a lithium-ion battery that is simulated using the aforementioned models.

2.1. 1D modified DualFoil model

Recently, Zhang et al. [31] reported a modified DualFoil model that incorporates mechanical deformation ensuing from lithium intercalation and externally applied elastic stress, and showed the importance of mechanical effects in battery simulation. In their work, the evolution of porosities of the electrodes/separator and the transport distance (coordinate transformation) of charged species are both considered. However, the overall thickness change of cells with graphite anodes during normal operation is usually within 3% [31,32,36,37]. The effect of coordinate transformation is relative small in such low-deformation simulations and the dominant contribution of mechanics comes from changes in porosities. In addition, we found that the coordinate transformation led to instabilities in high-rate charging simulations. Therefore, in this work, we only consider the mechanical effects on the porosity change, which will further significantly impact the kinetics of the battery system.

Porosity $\epsilon_{\rm e}$ is defined as the volume fraction of the electrolyte. As shown in Table 1, kinetic parameters like the effective diffusion coefficients and the effective electrolyte/electronic conductivity are functions of porosity and can be computed through the Bruggeman relation [38] as

$$(\cdot)_{\text{eff}} = (\cdot)\epsilon_e^{\alpha},$$
 (1)

where α is the Bruggeman's exponent.

For the sake of simplicity, side reactions are neglected and only the volume change of active materials and the volume change caused by externally applied elastic stress are considered [31]. By denoting $V_{\rm tot}$ as the total volume of the cell, $V_{\rm active}$ as the volume of the active materials, $\Delta V_{\rm elastic}$ as the volume change of the cell due to elastic deformation, the total volume change is described by the equation

$$\mathrm{tr}[\epsilon] = \frac{\Delta V_{\mathrm{active}}}{V_{\mathrm{tot}}} + \frac{\Delta V_{\mathrm{elastic}}}{V_{\mathrm{tot}}} = \frac{\overline{\Omega(C)} V_{\mathrm{active}}}{V_{\mathrm{tot}}} + \frac{\sigma}{E} = \overline{\Omega(C)} \epsilon_{\mathrm{active}}^0 + \frac{\sigma}{E}, \quad (2)$$

where $\mathrm{tr}[\varepsilon]$ is the total volume change, $\overline{\varOmega(C)}$ is the average volume change rate of the active materials, $\epsilon^0_{\mathrm{active}}$ is the initial volume fraction of the active materials, σ represents the externally applied stress, and E represents the Young's modulus. In this work, we assume that the electrolyte is incompressible and can only flow in the thickness direction of the cell [31]. Therefore, the porosity of the electrode region can be updated as

$$\epsilon_{\rm e} = \frac{1 - \epsilon_{\rm add}^0 - \epsilon_{\rm active}^0}{1 + {\rm tr}[\epsilon]} = \frac{\epsilon_{\rm e}^0}{1 + {\rm tr}[\epsilon]},\tag{3}$$

Table 1Summary of equations used to describe the involved physics in the model [29]

Equation description	Equations	
Electrolyte material balance	$\frac{\partial (\epsilon_{\rm e} c_{\rm e})}{\partial t} = \nabla \cdot \left(D_{\rm e,eff} \nabla c_{\rm e} + \frac{i_{\rm e} (1 - t_{+})}{F} \right)$	(7)
Electrolyte-phase Ohm's law	$i_{\rm e} = -\kappa_{\rm e,eff} \nabla \phi_{\rm e} + 2 \frac{\kappa_{\rm e,eff} R \theta}{F} (1 - t_{+}) \left(1 + \frac{\partial \ln f_{+}}{\partial \ln c_{-}} \right) \nabla \ln c_{\rm e}$	(8)
Intercalate material balance	$\frac{d}{dt}\bar{c} + 3\frac{j_n}{R_n} = 0$	(9)
Volume-averaged flux relation	$\frac{d}{dt}\bar{c} + 3\frac{j_n}{R_p} = 0$ $\frac{d}{dt}\bar{q} + 30\frac{D_n}{R_n^2}\bar{q} + \frac{45}{2}\frac{j_n}{R_n^2} = 0$	(10)
Intercalate boundary conditions	$35 \frac{D_s}{R_a} (c_s - \bar{c}) - 8 D_s \bar{q} = -j_n$	(11)
Solid-phase Ohm's law	$i_{\rm s} = -\kappa_{\rm s,eff} abla \phi_{\rm s}$	(12)
Butler-Volmer insertion kinetics	$j_n = k_0 c_s^{\alpha_c} c_e^{\alpha_a} \left(c_s^{\text{max}} - c_s \right)^{\alpha_a} \left[\exp \left(\frac{\alpha_a F}{R\theta} \eta_s \right) - \exp \left(- \frac{\alpha_c F}{R\theta} \eta_s \right) \right]$	(13)
Charge conservation	$\nabla \cdot (i_s + i_e) = 0$ with $\nabla \cdot i_e = -a_0 F j_n$	(14)

where $\epsilon_{\rm add}^0$ is the initial volume fraction of the additive materials and $\epsilon_{\rm e}^0$ is the initial porosity.

As the separator does not contain any active materials, the total volume change only consists of the elastic volume change given by

$$tr[\varepsilon] = \frac{\Delta V_{elatic}}{V_{tot}} = \frac{\sigma}{E}.$$
 (4)

Similarly, the porosity of the separator region can be updated as

$$\epsilon_{\rm e} = \frac{1 - \epsilon_{\rm solid}^0}{1 + {\rm tr}[\epsilon]} = \frac{\epsilon_{\rm e}^0}{1 + {\rm tr}[\epsilon]},\tag{5}$$

where $\epsilon_{\rm solid}^0$ is the initial volume fraction of solids.

The anode surface overpotential is calculated as

$$\eta_{\rm S} = \phi_{\rm S} - \phi_{\rm e} - U_{\rm S},\tag{6}$$

where $\eta_{\rm S}$ is the anode surface overpotential, $\phi_{\rm S}$ is the solid-phase potential, $\phi_{\rm e}$ is the electrolyte-phase potential, and $U_{\rm S}$ is the solid-phase open-circuit potential.

2.2. 3D Electro-chemo-thermo-mechanical model

Following Zhang et al. [32], the 3D electro-chemo-thermo-mechanical model is a 3D thermomechanical model based on finite strain theory coupled to the 1D modified DualFoil model described in Section 2.1.

For the sake of computation, the whole cell is divided into multiple sub-cells. For the 3D thermomechanical model, each electrochemical sub-cell is mapped to a group of adjacent thermomechanical elements, and its states are updated on each timestep using the 1D modified DualFoil model. A space-based mapping scheme [29] maps each group of thermomechanical elements to the corresponding electrochemical element. At each time step, the two models are solved in a staggered way. In each group of thermomechanical elements, the volume-averaged stress projected in the thickness direction and the volume-averaged temperature are computed and passed on to the corresponding electrochemical element. After updating the temperature and stress in the electrochemical element, the necessary outputs such as voltage, swelling ratio and heat generation rate, which are sent back to the corresponding thermomechanical elements for the next time step, are computed by the 1D modified DualFoil model. More details about the interface between the 1D electrochemical model and the 3D thermomechanical model can be found in [32].

Due to the volume change in each sub-cell, we must ensure that the volume integral of the output volumetric current densities matches the applied cell current. Our model iteratively updates the electric potential of all the sub-cells to satisfy this constraint at each time step. The simulation flow works in the following way:

- 1. Read input parameters and initialize the model with appropriate initial state variables.
- 2. Perform the staggered simulation for one new time step.
 - (a) Update the mechanical loading (mechanical boundary conditions and swelling ratio) and the thermal loading (thermal boundary conditions and heat generation rate) from the initial condition or the last time step.
 - (b) Solve the displacement field and the temperature field in the 3D thermomechanical model with the current swelling ratio and heat generation rate.
 - (c) Compute the projected stress and temperature for each sub-cell and update the corresponding state variables in the 1D electrochemical model.
 - (d) Guess a value of the cell voltage and assign it to each electrochemical element and then perform 2(d)i through 2(d)iii until convergence is reached.
 - Independently solve each electrochemical element in the constant-potential mode, and generate current densities of each electrochemical element.
 - ii. Compute the total current by summing over the current of each sub-cell and check if it matches with applied total current. The current of each sub-cell is calculated by multiplying the volumetric current density with its current volume.
 - iii. If the relative error of the total current is no less than the tolerance (we use 1e-8), adjust the voltage using the Newton–Raphson method with the derivative $\mathrm{d}V/\mathrm{d}I_{\mathrm{sum}}$ numerically calculated from previous iterations, and repeat steps 2(d)i and 2(d)ii.
 - (e) Once converged, update the swelling ratio and the heat generation rate for the associated thermomechanical elements of each sub-cell, wherein the displacement field and the temperature field for the next time step are computed.
- 3. Repeat step 2 until a specified cutoff potential is reached.

2.3. Model parameterization

We apply the models discussed in Sections 2.1 and 2.2 to study the thermal and mechanical effects on lithium plating in a prismatic cell. The cell consists of a graphite anode, a NCM811 cathode, a Celgard 2320 separator, and a 1M LiPF $_6$ salt in EC/DMC electrolyte.

Table 2Cell sandwich parameters used in all the test cases. The electrode parameters and activation energies are adopted from Kim et al. [30] unless otherwise noted. AE represents activation energy.

Parameters	$\text{Li}_x \text{C}_6$	Celgard 2320	NCM811
Thickness, µm	87.5	20	70.7
Electrolyte volume fraction	0.25	0.39	0.2
Inert filler volume fraction	0.1225		0.2058
Diffusion coefficient in slid, m ² /s	9.88e-15		1e-13 [39]
Film resistance, Ω m ²	0.002		0.001
D50 particle radius, μm	5		5.5
Reaction rate constant, mol/(m ² s)	4.4e-10		1e-12
Density, g/cm ³	2.2		4.8 [40]
Specific capacity, mAh/g	372		275.5
Matrix conductivity, S/m	100		100
Initial values of x and y	0.01		0.93
Bruggeman exponent	2.632 [45]	2.36 [47]	1.895[44]
Effective Young's modulus, N/m2	4.6e8 [43]	5.0e8 [43]	1.8e8 [42]
Salt concentration (LiPF6 in EC/DMC), M		1.0	
Solid state diffusion, AE, K	3500		2300
Insertion kinetics, AE, K	14,000		15,000
Film resistance, AE, K	4400		1300

Table 3

Expression for the electrolyte properties used in all the test cases [46]. The fitted coefficients can be found in Landesfeind and Gasteiger [46].

Property	Expression
Diffusion coefficient, cm ² /s	$p_1 \cdot \exp(p_2 \cdot c) \cdot \exp(\frac{p_3}{T}) \cdot \exp(p_4 \cdot c/T)$
Ionic conductivity, mS/cm	$q_1 \cdot (1 + (T - q_2)) \cdot c \cdot (1 + q_3 \sqrt{(c)} + q_4 \cdot (1 + q_5 \cdot \exp(\frac{1000}{T})) \cdot c) / (1 + c^4 \cdot (q_6 \cdot \exp(\frac{1000}{T})))$
Thermodynamic factor	$r_1 + r_2 \cdot c + r_3 \cdot T + r_4 \cdot c^2 + r_5 \cdot c \cdot T + r_6 \cdot T^2 + r_7 \cdot c^3 + r_8 \cdot c^2 \cdot T + r_9 \cdot c \cdot T^2$
Transference number	$s_1 + s_2 \cdot c + s_3 \cdot T + s_4 \cdot c^2 + s_5 \cdot c \cdot T + s_6 \cdot T^2 + s_7 \cdot c^3 + s_8 \cdot c^2 \cdot T + s_9 \cdot c \cdot T^2$

Table 4
Assumed mechanical and thermal properties of the cell [32].

Component	Material	Young's modulus [Pa]	Poisson's ratio	k [W/(m K)]	ho [kg/m ³]	c _p [J/(kg K)]
Jellyroll	Composite	3.08e8	0.01	in plane: 28 out of plane: 1.5	2708	781
Housing	Aluminum	6.9e10	0.334	202	2719	778
Tabs & terminals	Aluminum	6.9e10	0.334	202	2719	778
	Copper	1.21e11	0.34	386	8960	380
Current collectors	Aluminum	6.9e10	0.334	202	2719	778
	Copper	1.21e11	0.34	386	8960	380
Cap	HDPE	6.0e8	0.46	0.4	960	2054

The material properties of the components used in this model are obtained from previous studies [29,30,32,39–45], and are summarized in Table 2. The electrolyte properties can be found in Table 3, which are presented in [46]. The graphite open-circuit potential (OCP) was taken from Ref. [30] and the NCM811 OCP was measured for the present work (see details in B).

The cell geometry used in the 3D simulations, as shown in Fig. 1, is meshed with 831,387 thermomechanical elements. The cell consists of four jellyrolls and each jellyroll has a shape corresponding to two half cylinders on either end of a prismatic part. Stress concentration is expected to occur in the cylindrical regions due to the curved geometry of the jellyroll [32]. Therefore, each thermomechanical element in these regions is mapped to one electrochemical element, so as to better capture the mechanical effects. For the prismatic part of the jellyrolls, the assignment of sub-cells is based on the gradient of temperature, as the stress distribution is mostly uniform. Specifically, the size of the sub-cells in one direction is inversely correlated with the gradient of temperature in this direction. Furthermore, as our parallel computing algorithm adopts distributive memory, each processor owns only part of the mesh, so some sub-cells will be further divided by different processors in the thermomechanical domain. Overall, the four jellyrolls are modeled with 6863 sub-cells, each consisting of one electrochemical element.

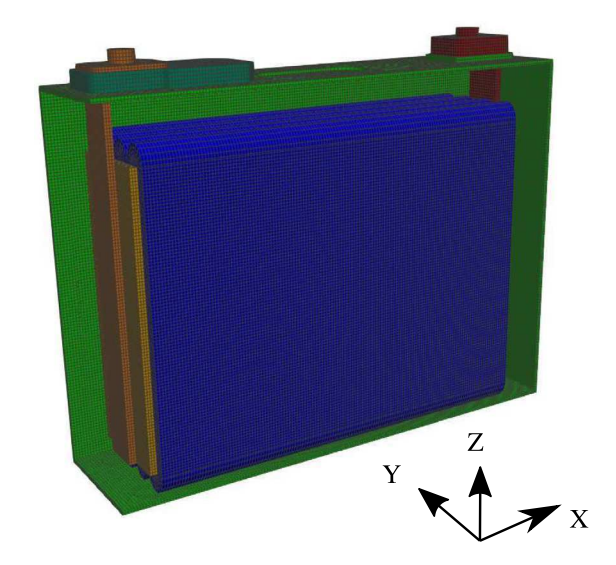
The mechanical and thermal parameters of each domain are summarized in Table 4 [32]. For the sake of simplicity, perfect thermal

contact is assumed on the interfaces between different components that are mechanically attached. Following [43], the homogenized Young's modulus of the jellyroll in Table 4 is computed via Voigt averaging as follows

$$E = L \cdot \left(\sum_{i} \frac{L_{i}}{E_{i}}\right)^{-1} \tag{15}$$

where L is the total thickness of the jellyroll and L_i is the thickness of each component of the jellyroll. Except for the jellyrolls, all other components are modeled by materials with isotropic thermal conductivity. As a jellyroll is generally made up of a wound multi-layer stack, it is modeled with anisotropic thermal conductivity: 28 W/(m K) for in-plane and 1.5 W/(m K) for out-of plane thermal conductivity [29]. In the horizontal cylindrical segments of the jellyrolls, 3D Cartesian coordinates are used to describe the thickness direction for assembling the thermal conductivity tensor of each thermomechanical element.

Regarding the mechanical boundary conditions, the cell casing is assumed to be fixed by five rigid end plates on five exterior flat surfaces (left, right, front, rear, and bottom). Forced convection with a heat transfer coefficient of 40 W/(m^2 K) is considered as the thermal boundary condition on all exposed surfaces of the cell. According to the functionality of different domains in the cell, the heat generation terms are computed in different ways. For the jellyrolls, the heat generation term is computed in the 1D electrochemical model from the internal impedances and current distributions of the component layers using



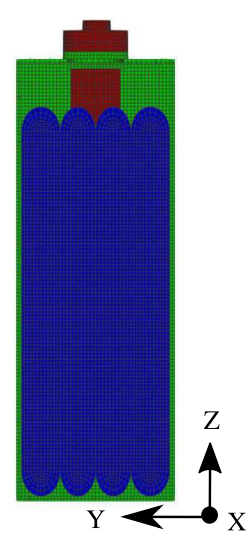


Fig. 1. Geometry of the lithium-ion battery. The size of the exterior casing is 172.5 mm L \times 45 mm W \times 140 mm H. The structure and components of the cell are listed as following: green, aluminum casing; blue, jellyrolls; yellow, copper current collector; orange, copper tab and terminal; red, aluminum tab and terminal; dark green, plastic. An additional aluminum current collector on the right side of the cell is obscured by the jellyroll. The space between the casing and the jellyrolls is assumed to be vacuum.

an energy balance derived in [48]. For the current collectors and the tabs, the Joule heating is computed in the 3D thermomechanical model, where the volumetric current density is assumed to be linearly distributed in the z direction. Specifically, the current density is zero at the bottom of the current collectors, and is equal to the applied current density at the top of the current collectors. All other domains are assumed to be electrically isolated and no heat generation terms are included.

3. 1D numerical results

In this section, we use the 1D modified DualFoil model, incorporating mechanical deformation as discussed in Section 2.1, to investigate the thermal and mechanical effects on lithium plating, which is indicated by the anode surface overpotential. As temperature and charging rates can have a significant impact on the battery performance, we run simulations and present the results considering three main scenarios summarized in Table 5: 1) 1C charge at an ambient temperature of 0 °C, as shown in Fig. 2; 2) 1C charge at an ambient temperature of 25 °C, as shown in Fig. 3; 3) 4C charge at an ambient temperature of 25 °C, as shown in Fig. 4. In each scenario, simulations are performed under either isothermal or nonisothermal conditions. Further, each case is investigated by either considering or ignoring mechanical deformations. For the isothermal simulations, the fixed temperature is obtained by the average temperature of the corresponding nonisothermal simulation, ignoring mechanical deformations, during the whole charging process. Specifically, the average temperatures of the nonisothermal simulations ignoring mechanical deformations for the three scenarios are 16 °C, 34 °C and 56.5 °C respectively. In addition, no external elastic stress is applied in the simulations considering mechanical deformation, and hence the porosity change is only affected by the volume change of the active materials during intercalation and deintercalation. The cutoff voltage is set as 4.2 V for all the tests.

3.1. Effects of thermal evolution on anode surface overpotential

To show the contribution of thermal evolution to the anode surface overpotential, we compare the results of the nonisothermal and isothermal simulations for the three scenarios in Table 5. Only simulations which ignore mechanical deformation are discussed, as similar trends can be observed in simulations that consider mechanical deformation.

Table 5
Summary of 1D simulation scenarios.

Scenario	Charging rate	Isothermal (w/ or w/o mech.) Fixed temperature	Nonisothermal (w/ or w/o mech.) Ambient temperature
1	1C	16 °C	0 °C
2	1C	34 °C	25 °C
3	4C	56.5 °C	25 °C

Fig. 2 shows the comparison between the 1C nonisothermal simulation (the blue line marked with asterisks) at an ambient temperature of 0 °C and its corresponding isothermal simulation (the green line marked with crosses). A temperature rise from 0 °C to 20 °C is observed for the nonisothermal case, with the average being 16 °C, which in turn is used as the fixed temperature for the isothermal case. From the voltage profile, one can observe that the nonisothermal case holds a higher voltage at the beginning of charging, but a lower voltage at the end. This behavior can be explained based on the lower temperature of the nonisothermal case, in comparison with the isothermal case, which leads to a higher impedance and thus a higher voltage. However, when the temperature increases, the impedance drops resulting in a lower voltage. The opposite trend can be seen in the anode surface overpotential curves. As charging commences, a lower anode surface overpotential is found in the nonisothermal case due to a lower temperature. However, when the temperature exceeds that used in the isothermal case, the anode surface overpotential becomes higher. Here, we define the term "plating onset SOC" as the state of charge (SOC) at which the anode surface overpotential drops below zero. As a result, the plating onset SOC in the isothermal case is 32.8%, while it is 37.9% in the nonisothermal case. Thus, an additional +5.1% of the cell's capacity can be charged until plating is observed by considering nonisothermal conditions; this result has been tabulated as shown in Table 6.

In Scenario 2, the ambient temperature is changed to 25 °C, while the charging rate is still set as 1C. As shown in Fig. 3, the temperature range during the charging process observed in the nonisothermal simulation is from 25 °C to around 37 °C, which is a smaller rise in comparison with Scenario 1. In the isothermal simulation, the temperature is fixed at 34 °C. Due to a smaller temperature difference in this scenario, both the cases predict similar voltage and anode surface overpotentials. The plating onset SOC in the nonisothermal case is around 62.8%, while that in the isothermal case is around 60.6%.

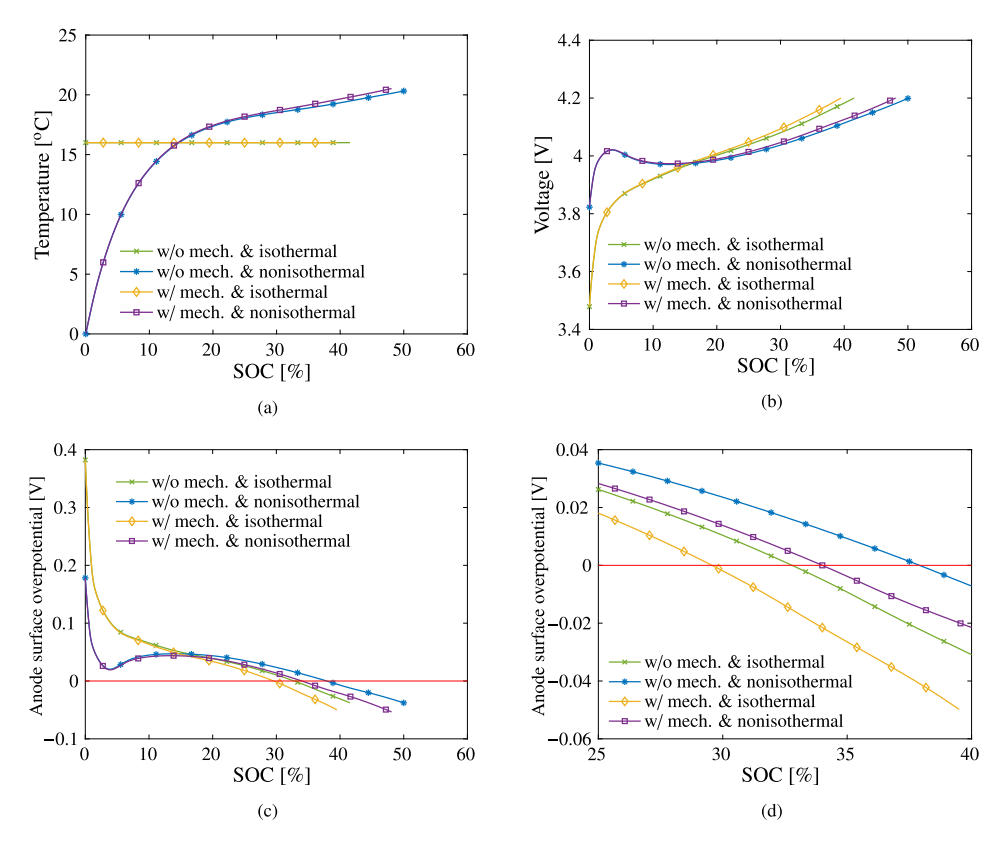


Fig. 2. 1D simulation results for Scenario 1: a) temperature versus SOC; b) voltage versus SOC; c) anode surface overpotential versus SOC; d) zoom-in version of (c).

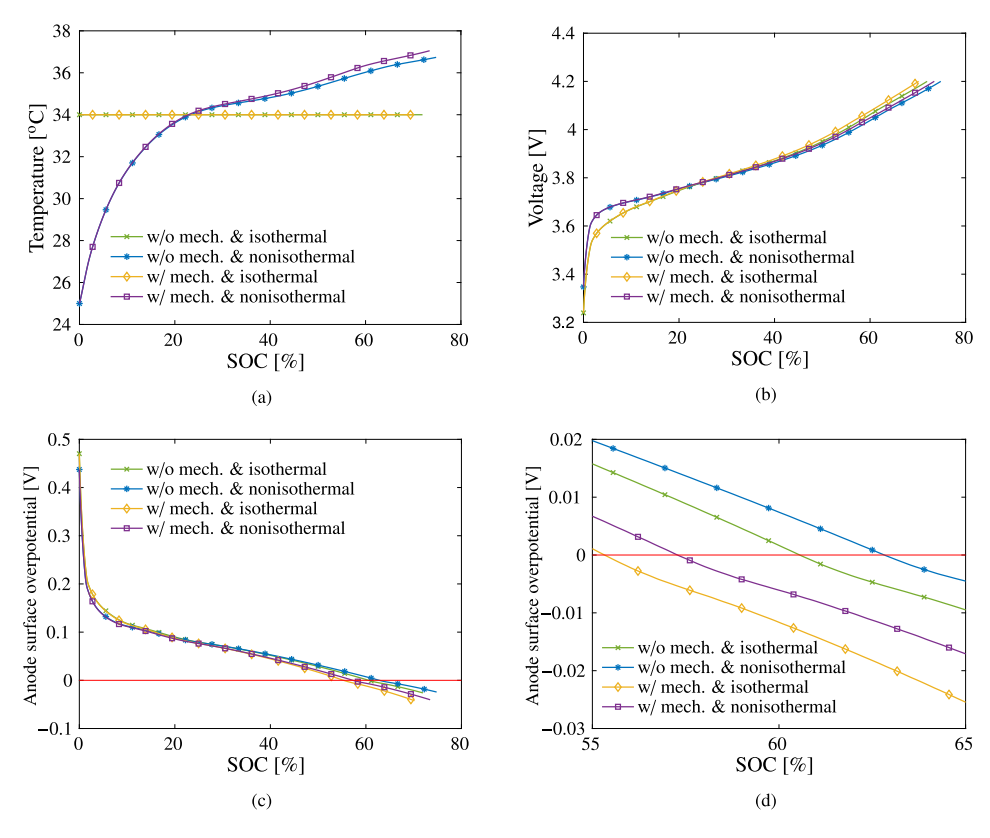


Fig. 3. 1D simulation results for Scenario 2: a) temperature versus SOC; b) voltage versus SOC; c) anode surface overpotential versus SOC; d) zoom-in version of (c).

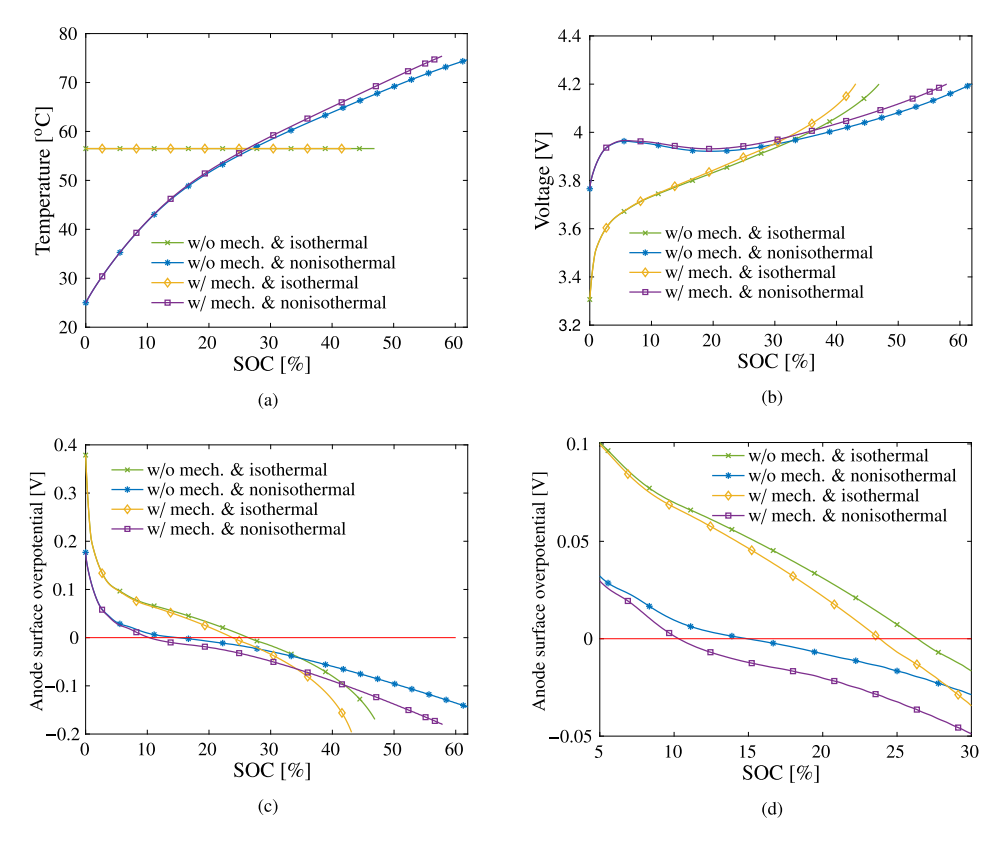


Fig. 4. 1D simulation results for Scenario 3: a) temperature versus SOC; b) voltage versus SOC; c) anode surface overpotential versus SOC; d) zoom-in version of (c).

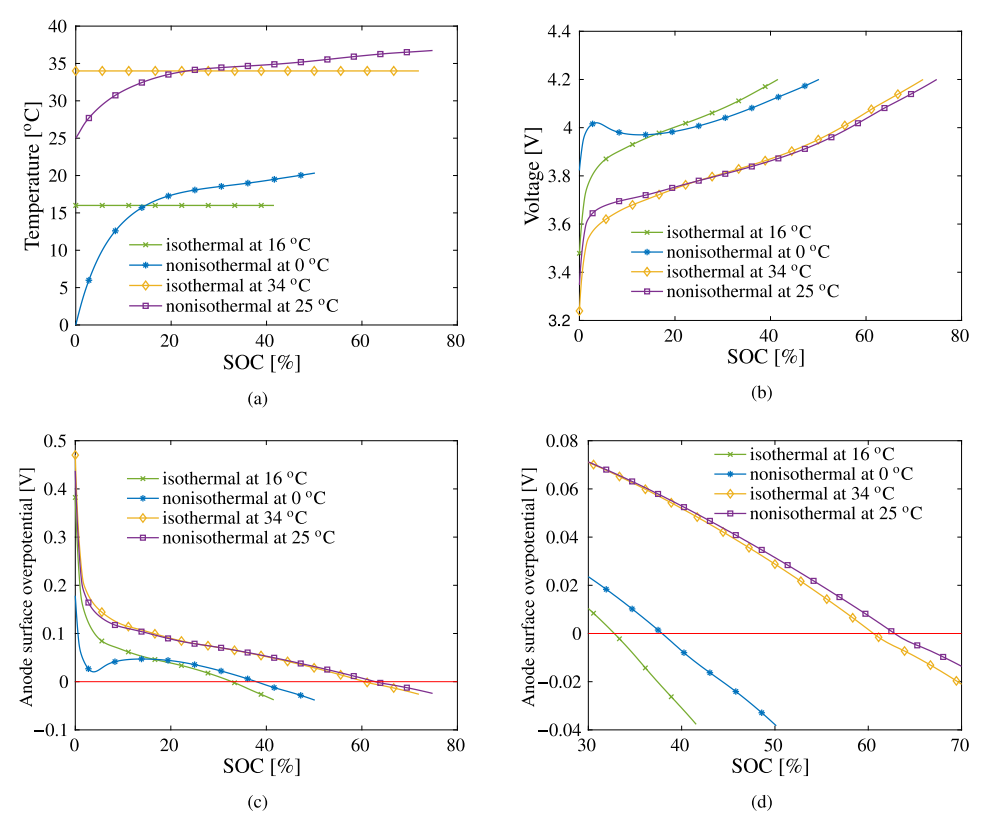


Fig. 5. 1D isothermal/nonisothermal 1C charging simulations without mechanical deformation at different temperatures.

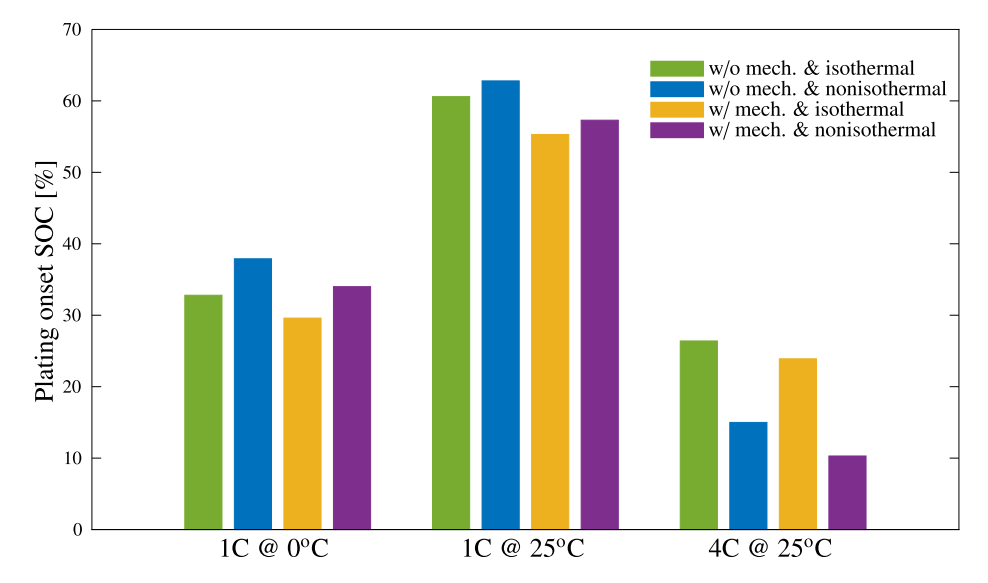


Fig. 6. Bar chart of plating onset SOC plotted with data in Table 6.

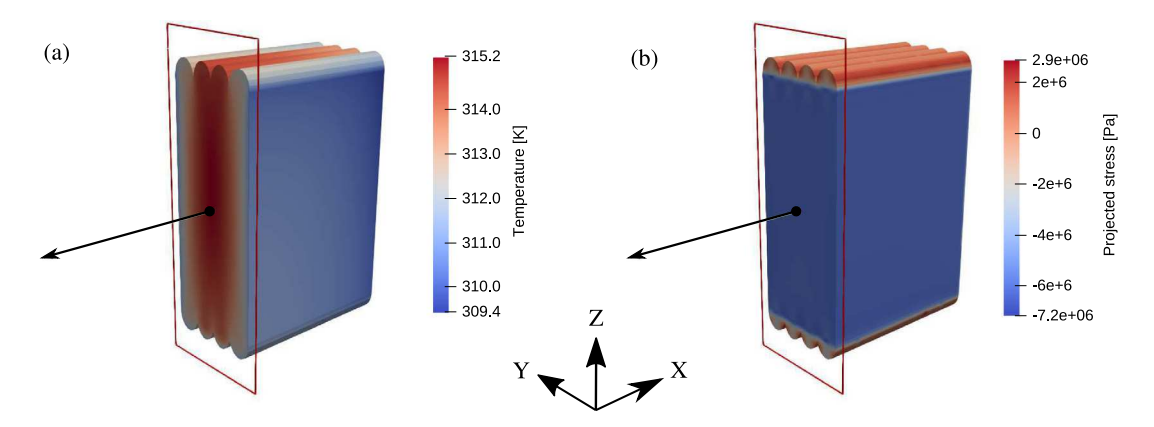


Fig. 7. 3D contour of (a) temperature and (b) projected stress in jellyrolls for the nonisothermal case considering mechanical deformation after being charged for 50 min. Only the right half of the jellyrolls is plotted, so as to show the distribution in the cross section in the y-z plane.

Therefore, considering nonisothermal conditions in Scenario 2 yields an additional +2.2% of the cell's capacity that can be charged before plating.

In the last scenario, we consider a 4C charging rate at an ambient temperature of 25 $^{\rm o}$ C and the results are shown in Fig. 4 (the green curve marked with crosses and the blue curve marked with asterisks). The temperature in the nonisothermal simulation (the blue curve marked with asterisks) increases from 25 $^{\rm o}$ C to around 75 $^{\rm o}$ C, with a span of around 50 $^{\rm o}$ C, while the temperature in the isothermal simulation is fixed at 56.5 $^{\rm o}$ C. This large temperature difference results in significant differences in the evolution of voltage and anode surface overpotential. The plating onset SOC is around 15% and around 26.4% in the nonisothermal and isothermal simulations, respectively. In this scenario, the difference in the plating onset SOC comes to 11.4%.

From the above scenarios, we can conclude that when the temperature rise is relatively small, isothermal and nonisothermal simulations yield very similar predictions of the plating onset SOC. However, when the temperature rise increases, one can see more significant effects of thermal evolution on the anode surface overpotential, and so nonisothermal simulations cannot be replaced by isothermal simulations. We also observe that a lower temperature usually corresponds to a lower anode surface overpotential. As the temperature of the isothermal simulations is the average of the temperature in the nonisothermal simulations, the latter always have a lower temperature and a lower anode surface overpotential at the beginning. The order is typically

flipped sometime after the temperature of the nonisothermal simulation exceeds that of the isothermal simulation.

3.2. Effects of lower temperatures on anode surface overpotential

In this subsection, we analyze the effects of lower temperatures on anode surface overpotential, ignoring mechanical deformation. The isothermal cases (1C charging at 16 $^{\rm o}$ C and 1C charging at 34 $^{\rm o}$ C) and the nonisothermal cases (1C charging at an ambient temperature of 0 $^{\rm o}$ C and 1C charging at an ambient temperature of 25 $^{\rm o}$ C) in Scenario 1 and Scenario 2 are compared in Fig. 5.

It is well established that the main components of cell impedance (ohmic and mass transfer impedance in the electrolyte, solid-phase mass transfer impedance, film resistance, and charge transfer resistance) increase in value as the temperature is decreased [50]. In the isothermal cases, though both are charged at 1C with the same material properties and cell design, the one at a lower temperature has a higher voltage due to its relatively high impedance. The case at 16 °C generally has a lower anode surface overpotential, which drops to zero at 32.8% SOC, while the plating onset SOC of the case at 34 °C is 60.6%. Hence, it is evident from the results that a lower temperature results in a 27.8% lower plating onset SOC for the isothermal case as compared to the higher temperature.

The nonisothermal cases report different temperature evolutions, with the case at an ambient temperature of 25 °C remaining at a higher

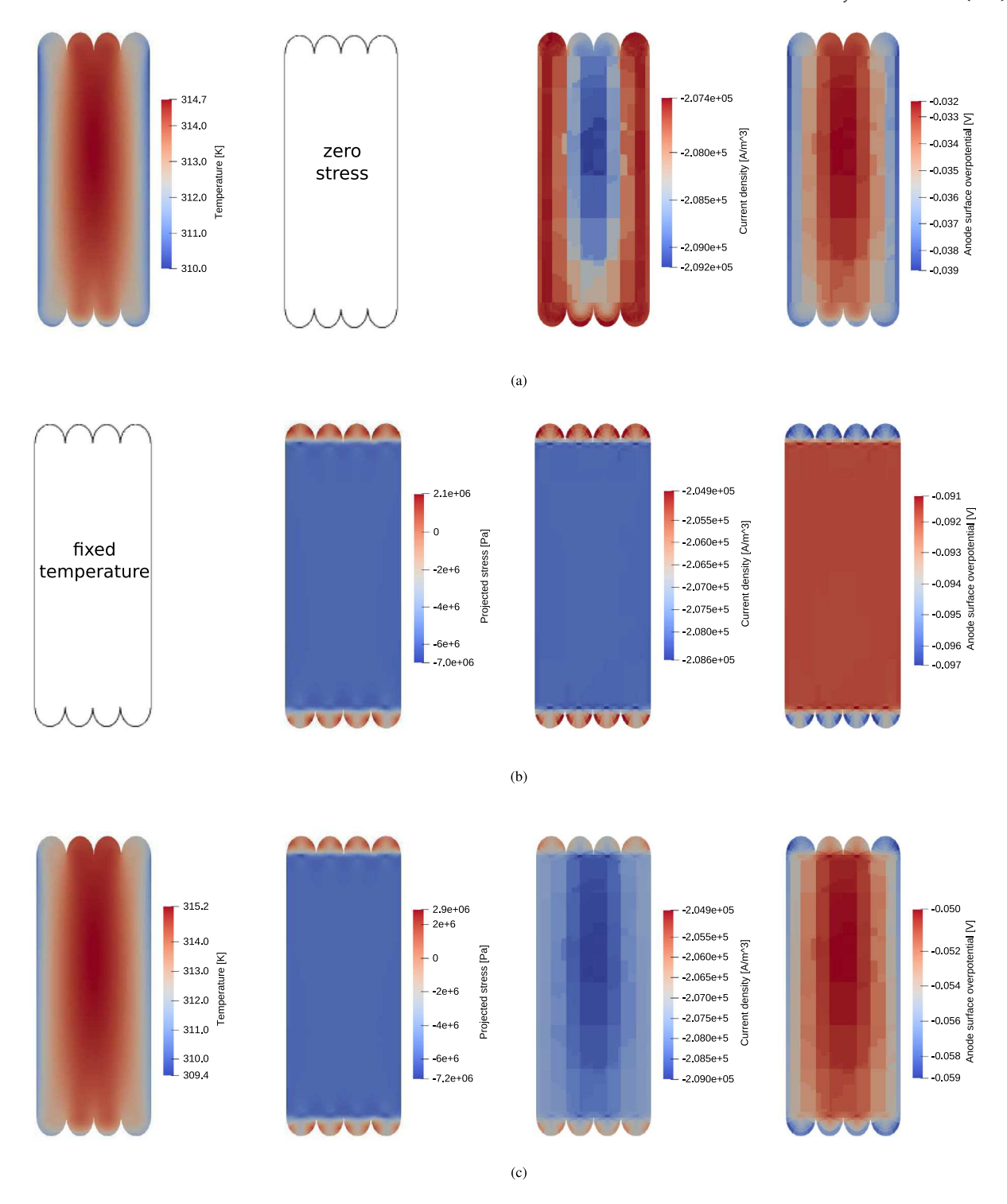


Fig. 8. 3D simulation results after 50 min of charging under: a) 1C nonisothermal conditions ignoring mechanical deformation; b) 1C isothermal conditions (34°C) considering mechanical deformation; c) 1C nonisothermal conditions considering mechanical deformation.

Table 6
SOC when the anode surface overpotential drops to zeroin each scenario, and the difference compared with the isothermal case without mechanical deformation. Here "w/o mech." represents the case not considering mechanical deformation, and "w/ mech." for the case considering mechanical deformation.

Cases	w/o mech. & isothermal	w/o mech. & nonisothermal	w/ mech. & isothermal	w/ mech. & nonisothermal
1C @ 0 °C	32.8% (+0%)	37.9% (+5.1%)	29.6% (-3.2%)	34.0% (+1.2%)
1C @ 25 °C	60.6% (+0%)	62.8% (+2.2%)	55.3% (-5.3%)	57.3% (-3.3%)
4C @ 25 °C	26.4% (+0%)	15.0% (-11.4%)	23.9% (-2.5%)	10.3% (-16.1%)

Fig. 9. Experimental results of lithium deposits on anodes after 115 cycles of a model-based fast-charging protocol (MOD_{cyc} protocol) [49]. Very large localized deposits of lithium can be observed in the folds of the anodes. Marked red boxes refer to the terminal tab imprints that are not modeled or captured in the present work. Reproduced with permission from [49].

temperature in comparison with the one at an ambient temperature of 0 $^{\circ}$ C. Similar to the findings in the isothermal cases, the former with a higher temperature has a lower voltage and a higher anode surface overpotential than the latter. Consequently, a 24.9% lower plating onset SOC results from a lower ambient temperature for the nonisothermal case.

Therefore, both the isothermal and nonisothermal cases show significant effects on the anode surface overpotential profile of cells due to the presence of a lower temperature. Keeping cells at appropriate temperatures (e.g., between 15 $^{\rm o}$ C and 35 $^{\rm o}$ C [51]) can decrease the risk of lithium plating and further enhance the durability of cells.

3.3. Mechanical effects on anode surface overpotential in isothermal conditions

In order to investigate specifically the mechanical effects on the performance of the cell, we compare the simulation results considering mechanical deformation (the yellow line marked with diamonds) with those ignoring mechanical deformation (the green line marked with crosses) in isothermal conditions. As mentioned at the beginning of this section, the temperature of the isothermal simulations in Scenarios 1, 2, and 3, are 16 °C, 34 °C and 56.5 °C, respectively. In all the scenarios, the differences in the anode surface overpotential between the simulations considering mechanical deformation and those ignoring mechanical deformation are observed to increase as the SOC increases.

In Scenario 1, as shown in Fig. 2, the anode surface overpotential curves of both cases almost overlap in the first 15% SOC. However later, the anode surface overpotential for the case considering mechanical deformation starts to drop faster than that for the case ignoring it, finally leading to a maximal difference in anode surface overpotential of 0.021 V at 39.5% SOC. Further, it can be observed that the plating onset SOCs of the cases considering and ignoring mechanical deformation are 29.6% and 32.8%, respectively. Thus, accounting for mechanical deformation can lead to around 3.2% decrease in the plating onset SOC.

In Scenario 2, the anode surface overpotential curves of both cases remain similar in the initial phase till 20% SOC, as shown in Fig. 3. Similar to Scenario 1, the anode surface overpotential for the case considering mechanical deformation decreases faster, and the maximal surface overpotential difference is 0.0208 V at 70.2% SOC. However, the plating onset SOCs of the cases considering and ignoring mechanical deformation are 55.3% and 60.6% respectively, leading to a 5.3% decrease by considering mechanical deformation.

In Scenario 3, the anode surface overpotential curves deviate earlier than the last two scenarios. The maximal surface overpotential difference is noted as 0.083~V at 43.1% SOC. The plating onset SOC of the case considering mechanical deformation is 23.9%, which is 2.5% ahead of the case ignoring mechanical deformation.

In these three scenarios, once the charging rates and the temperature are determined, the evolution of the anode surface overpotential curve is also determined. The effect of mechanical deformation will distort the curve a bit, leading to a difference in plating onset SOC. Because of different rates of change in the anode surface overpotential in different scenarios, the surface overpotential difference is more a

combination of the effects of charging rate, temperature, and mechanical deformation. As the mechanical effects in our model originate from the volume change of the active materials, an increasing amount of lithium transported amplifies the impact of mechanics. Scenario 1 and Scenario 2 have very close maximal surface overpotential differences, but the plating onset SOC difference is much larger in Scenario 2. A major reason for this observed behavior is that although the rate of change in anode surface overpotential is smaller in Scenario 2, the larger amount of lithium transported leads to larger mechanical effects. In scenario 3, although the rate of change in anode surface overpotential is the largest, the fact that only a small amount of lithium is transported results in the maximal surface overpotential difference being the largest, but plating onset SOC difference being the smallest.

3.4. Mechanical effects on anode surface overpotential in nonisothermal conditions

Mechanical effects on anode surface overpotential in nonisothermal conditions are studied in this subsection, by comparing the cases considering mechanical deformation (the purple curve marked with squares) with those ignoring mechanical deformation (the blue curve marked with asterisks) in nonisothermal conditions. We observe that there is a slight difference in the temperature evolution between the two cases as mechanical deformation affects electrical responses which further leads to different heat generation rates. From the plot of the anode surface overpotential, one can observe that mechanical deformation accelerates the drop of the anode surface overpotential, as we have seen in isothermal conditions. Furthermore, the differences in plating onset SOC between cases considering mechanical deformation and those ignoring it are also similar to those we noted in isothermal conditions, which are now around 3.9% for Scenario 1, 5.5% for Scenario 2, and 4.7% for Scenario 3.

3.5. Summary of the 1D results

In conclusion, a lower temperature and accounting for mechanical deformation can accelerate the reduction of anode surface overpotential to zero, which indicates the initiation of lithium plating. Table 6 and Fig. 6 summarize the plating onset SOC for each case. In each scenario, we set the result of the isothermal simulation ignoring mechanical deformation as the reference and quantify the effects in the other scenarios by the difference in those capacities with the reference one, which are reported in parentheses. The contribution of the thermal evolution mostly depends on the temperature range of the charging operation. In cases like Scenario 3, the thermal evolution has a nonnegligible impact, given a temperature rise as large as 50 °C, while in the other cases with smaller temperature rise, the thermal evolution has less effect on the anode surface overpotential. Mechanical deformation also has been observed to have significant impact on lithium plating. Mechanical effects are mostly determined by the amount of lithium transported from the cathode to the anode, which causes the volume change of active materials and subsequent decrease in anode porosity. Both thermal evolution and mechanical deformation should be considered for better accuracy of predicting the onset of lithium plating.

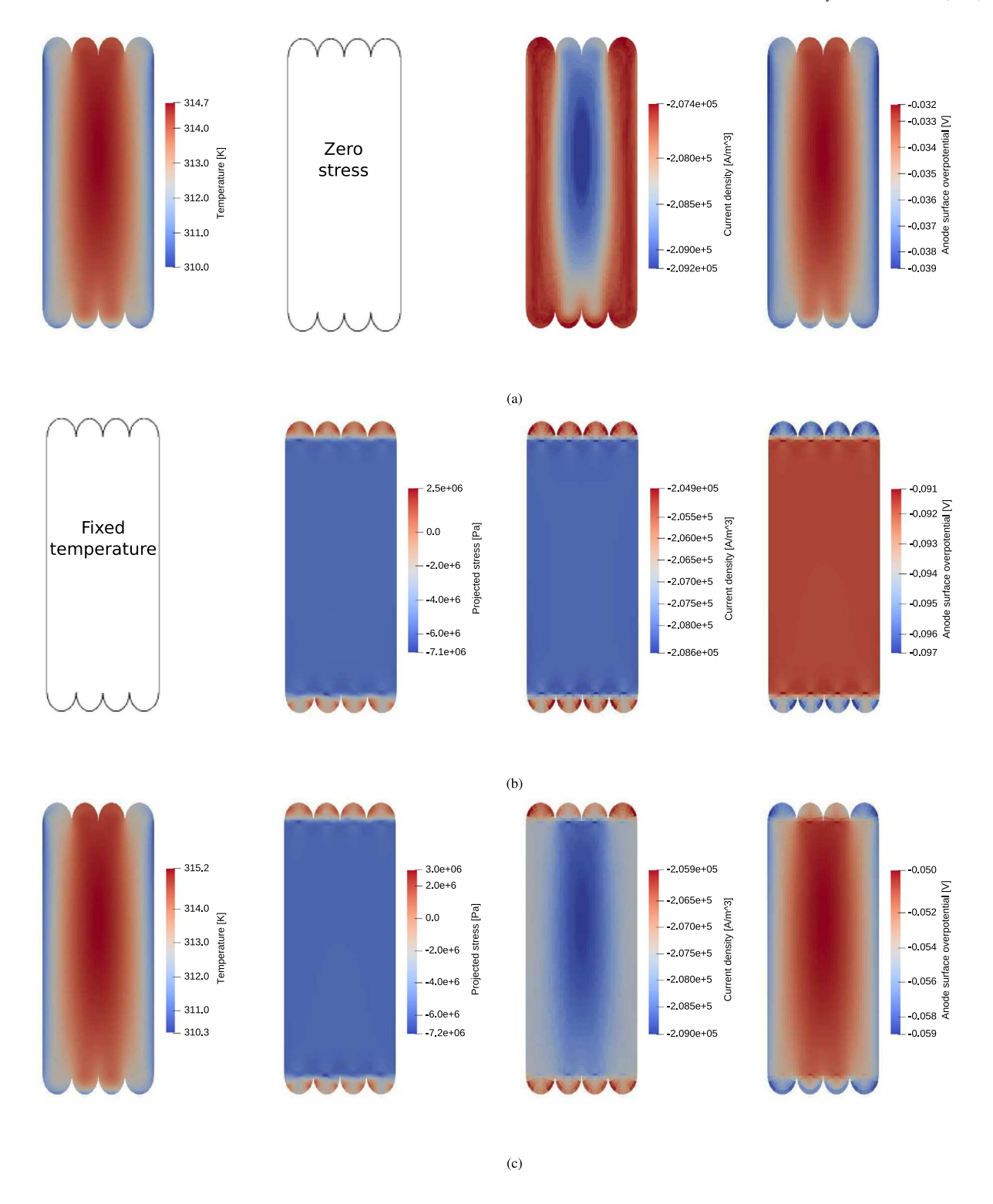


Fig. A.1. 3D simulation results with refined electrochemical mesh after 50 min of charging under: a) 1C nonisothermal conditions ignoring mechanical deformation; b) 1C isothermal conditions (34 °C) considering mechanical deformation; and c) 1C nonisothermal conditions considering mechanical deformation.

4. 3D Numerical results

Although the 1D model can efficiently simulate cell behavior, it assumes a uniform stress and temperature distribution in the whole cell. However, if the nonuniformity in either the stress or temperature distribution is significant, this model can lead to erroneous results. Alternatively, our 3D model can accurately capture the distribution of stress and temperature, thereby improving the accuracy when the stress

or temperature field is nonuniform. In addition, the 3D model can also visualize the distribution of the anode surface overpotential in the cell, which would be helpful in predicting the vulnerable regions for lithium plating.

In this section, the cell is charged at 1C for 50 min and three cases are investigated: a) in nonisothermal condition with an ambient temperature of 25 $^{\circ}$ C, ignoring mechanical deformation; b) in

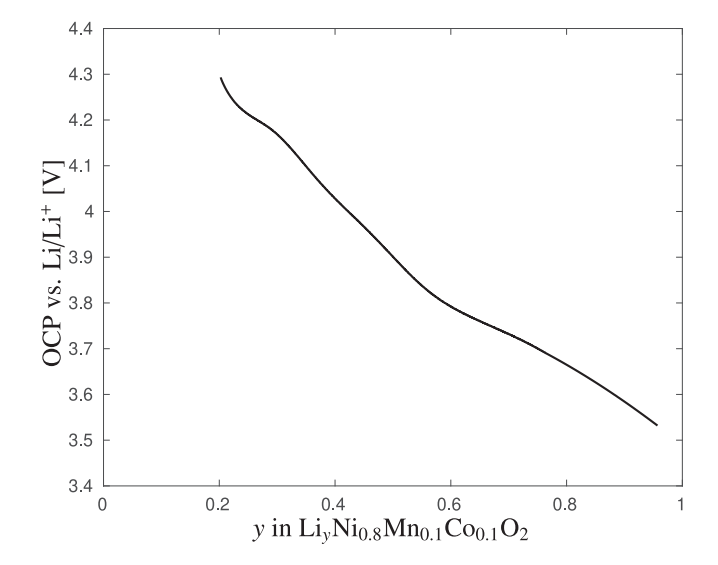


Fig. B.1. OCP curve of NCM811 obtained from a combination of slow cycling and galvanostatic intermittent titration technique (GITT) steps.

isothermal condition with a fixed temperature of $34\,^{\circ}\text{C}$, considering mechanical deformation; c) in nonisothermal condition with an ambient temperature of $25\,^{\circ}\text{C}$, considering mechanical deformation.

Fig. 7 shows the 3D contour of temperature and projected stress in jellyrolls for the nonisothermal case considering mechanical deformation after being charged for 50 min. To show the distribution of temperature and projected stress in the cross section in the y-z plane (as shown in the red box), only half of the jellyroll region is plotted. Fig. 7(a) shows the temperature profile of the jellyrolls, where one can observe that temperature is nonuniform along the y direction, but nearly uniform along the x and z directions. A main reason for this is that the thermal conductivity in the y direction is primarily throughplane (1.5 W/(m K)), whereas the conductivity in the x and z directions is primarily in-plane (28 W/(m K)). The projected stress in the thickness direction is plotted in Fig. 7(b). The thickness direction of the prismatic part is in y direction and compressive stress is observed due to the overall swelling of the jellyrolls during charging. However, due to the geometry of the prismatic cell, tensile stress arises in the cylindrical regions of the jellyrolls. Therefore, the differences in the projected stress mostly depend on the geometry of the jellyroll, and are more significant in the z direction. As the nonuniformity of temperature and stress is along the y and z directions, respectively, we will focus on the contours in the y - z plane in our following analysis.

The results for the three cases using the 3D model are presented in Fig. 8, which consist of the contours for temperature, projected stress in the thickness direction, current density and anode surface overpotential. Fig. 8(a) illustrates the results for the nonisothermal case ignoring mechanical deformation. As the mechanical deformation is ignored, all the spatial differences in the contour originate from the nonuniformity in the temperature distribution. Owing to the thermal convection from the cell exterior, the temperature at the central part is higher than that at exterior surfaces. Due to the higher temperature at the central part, the impedance is lower and hence the current density is higher. From the contour of the anode surface overpotential, one can observe that lithium plating is more likely to occur on the exterior surface due to its lower temperature.

The results for the isothermal case considering mechanical deformation are shown in Fig. 8(b). As the isothermal condition is assumed, the nonuniformity in the current density and the anode surface overpotential is affected by the difference in the projected stress in the thickness direction. As the cell is charged, the cell sandwich thickness tends to increase due to higher anode active material swelling relative to cathode active material contraction. Swelling in the prismatic portions of the jellyrolls, which due to mechanical constraints are under compression,

puts tension on the folds (cylindrical regions) in both circumferential and radial directions. The net tensile stress (orthogonal to cell sandwich plane) in cylindrical regions relative to prismatic regions results in a relatively greater volume (thickness) increase in the cylindrical regions, which in turn implies a greater drop in anode porosity, and hence higher ionic transport resistance. Therefore, the anode surface overpotential tends to be lower in the cylindrical than the prismatic portions of the jellyrolls, resulting in a relatively higher driving force for Li plating in these regions. Experimental observations consistent with this result are shown in Fig. 9, where a significant amount of deposited lithium can be seen in the folds of the anode after 115 cycles of a model-based fast-charging protocol (MOD_{cyc} protocol) [49]. Marked red boxes indicate the terminal tab imprints, which are not captured in the present work, although mechanics (anode compression, reduced porosity) could play a factor in the Li deposition observed there.

The last case considers mechanical deformation in a nonisothermal simulation. Similar to the first case, lower temperature is observed at the exterior surface of the jellyrolls. The stress distribution is similar to that in the second case. Therefore, the spatial difference in the electrochemical response can be regarded as a combination of the nonuniformity of both temperature and stress. The contour of the anode surface overpotential shows that the lowest anode surface overpotential exists on the exterior surface of the horizontal cylindrical segments of the leftmost and rightmost jellyrolls. In comparison with the first case, which ignores mechanical deformations, the span of the anode surface overpotential increases from 7 mV to 9 mV, and the minimum is 20 mV lower, indicating the significant effect of mechanical deformation.

These findings point to the need for either incorporating more accurate models into battery management systems that utilize advanced charging algorithms to avoid lithium plating and other aging mechanisms, or to increase the error margin to account for mechanical, thermal, and spatial effects. As it is not yet tractable to incorporate a 3D+1D model as described here in real-time battery control units, the latter approach is recommended. The margin for error could be analyzed in offline simulations and incorporated into online algorithms as lookup tables, neural networks, or otherwise simplified surrogate models.

5. Conclusion

Lithium plating consumes cyclable lithium and hence is one of the main concerns for cell durability. Both the thermal and mechanical effects play an important role in the initiation of lithium plating in lithium-ion batteries. A 1D model and a 3D model introduced previously [31,32] are employed to investigate these effects. The 1D model accounts for the mechanical effects due to lithium intercalation and externally applied pressure. The 3D model incorporates the 1D model and further describes the nonuniformity of temperature and stress in cells. We compute the anode surface overpotential as an indicator for the initiation of lithium plating, with a more negative anode surface overpotential representing a higher driving force for lithium plating. Our 1D model shows that lithium plating is more likely to occur at lower ambient temperatures and at higher charging rates. Additionally, it is observed that mechanical deformation can accelerate the initiation of lithium plating, thus corroborating the importance of considering mechanical deformation in lithium plating analysis. Although the 1D model assumes a uniform temperature and stress distribution in the body, the 3D model is able to capture the effects of nonuniformity. Because of the thermal convection on the exterior surface of the cell, a lower temperature is observed there, leading to a lower anode surface overpotential. The geometry of the prismatic cell results in a tensile stress in the cylindrical regions (folds) of the jellyrolls due to the swelling of the cell, which further decreases the anode surface overpotential. All in all, our model qualitatively and quantitatively estimates the impact of internal cell heating, nonuniform temperature, and mechanical deformation on the initiation of lithium plating, and demonstrates the importance of their inclusion in lithium plating analysis, particularly in advanced charging algorithms and cell design. Future work considering the lithium plating side reaction itself is essential to better quantify cell durability. In addition, a more comprehensive model is needed for large scale batteries to account for the electrolyte flow caused by nonuniform electric field and mechanical pressure.

CRediT authorship contribution statement

Yitao Qiu: Conceptualization, Methodology, Software, Formal analysis, Writing - original draft. Xiaoxuan Zhang: Methodology, Software, Validation, Writing - review & editing. Camille Usubelli: Investigation. Daniel Mayer: Software. Christian Linder: Resources, Writing - review & editing, Funding acquisition, Supervision. Jake Christensen: Conceptualization, Methodology, Validation, Formal analysis, Writing - review & editing, Supervision.

Declaration of competing interest

The authors declare that they have no known competing financial interests or personal relationships that could have appeared to influence the work reported in this paper.

Acknowledgments

Yitao Qiu and Christian Linder acknowledge funding for this work from the US National Science Foundation under Contract Number CMMI-1911836 and from the Stanford StorageX Initiative.

The electrodes were produced at the U.S. Department of Energy's (DOE) CAMP (Cell Analysis, Modeling and Prototyping) Facility, Argonne National Laboratory. The CAMP Facility is fully supported by the DOE Vehicle Technologies Program (VTP) within the core funding of the Applied Battery Research (ABR) for Transportation Program.

Appendix A. 3D Numerical results with refined electrochemical mesh

The ratio of thermomechanical to electrochemical elements is set as 1:1 to produce more smooth contour plots in y - z plane for 3D simulations, as shown in Fig. A.1. The total number of electrochemical elements is 94603. The ranges of the outputs are very close to those in Fig. 8, which validates our results in Section 4.

Appendix B. Electrode properties measurement

The open-circuit potential (OCP) curve of NCM811, shown in Fig. B.1, was obtained from a combination of slow cycling and galvanostatic intermittent titration technique (GITT) steps. In a first step, slow C/50 charge and discharge were averaged in a trust region where the capacity accessed is not dependent on the C-rate applied (from 4.3 V to 3.7 V for NCM811). The material was then characterized at higher lithiation content with GITT steps consisting of short current pulses and long rest periods to access the equilibrium potential of the material. The combination of the two steps, detailed in a future publication, allows for this method to characterize the OCP vs Li content relation up to x_{Li}

List of symbols

```
initial active interfacial area per unit electrode volume
(specific interfacial area), m-1
```

- volume-averaged solid-phase Li concentration, mol m⁻³ \bar{c}
- $\mathrm{Li^{+}}$ concentration of electrolyte, mol $\mathrm{m^{-3}}$ $c_{\rm e}$
- surface solid-phase Li concentration, mol $\rm m^{-3}$
- maximum surface solid-phase Li concentration, mol m⁻³
- \tilde{D}_{ς} solid-phase diffusion coefficient, m² s⁻¹
- $D_{\rm e,eff}$ effective electrolyte diffusion coefficient, m² s⁻¹
- E Young's modulus, N m^{−2}
- salt activity coefficient f_{\pm}
- Faraday's constant, 96 485 C mol⁻¹
- electrolyte-phase current density, A m⁻² i_e
- solid-phase current density, A m⁻² i_s
- pore-wall flux across interface in the reference configuration, j_n $mol m^2 s^{-1}$
- reaction rate constant, m^{3/2} s⁻¹ mol^{-1/2} k_0
- volume-averaged solid-phase Li concentration gradient, $mol m^{-4}$
- gas constant, $8.314 \text{ J mol}^{-1} \text{ K}^{-1}$ R
- R_n radius of solid particles, µm
- time, s
- cationic transference number t_{\perp}
- solid-phase open-circuit potential, V $U_{\rm s}$
- Vvolume
- α Bruggeman exponent
- anodic transfer coefficient α_a
- cathodic transfer coefficient
- initial volume fraction of active materials
- $\epsilon_{
 m activ}^{
 m 0}$ initial volume fraction of additive materials
- volume fraction of electrolyte
- ϵ_{e} $\epsilon_{\mathrm{e}}^{0}$ $\epsilon_{\mathrm{solid}}^{0}$ initial volume fraction of electrolyte
- initial volume fraction of solids
- surface overpotential, V
- strain field
- $\kappa_{\rm e,eff}$ effective electrolyte conductivity (Li⁺), S m⁻¹
- $\kappa_{s,eff}$ effective electronic conductivity (e⁻), S m⁻¹
- electrolyte-phase potential, V
- solid-phase potential, V $\phi_{\rm s}$
- homogenized Cauchy stress, N m⁻²
- temperature, K
- $\overline{\Omega(C)}$ average volume change rate of active materials

References

- [1] R. Borah, F. Hughson, J. Johnston, T. Nann, On battery materials and methods, Mater. Today Adv. 6 (2020) 100046.
- X. Han, L. Lu, Y. Zheng, X. Feng, Z. Li, J. Li, M. Ouyang, A review on the key issues of the lithium ion battery degradation among the whole life cycle, ETransportation 1 (2019) 100005.

- [3] P. Nakhanivej, H.H. Rana, H. Kim, B.Y. Xia, H.S. Park, Transport and durability of energy storage materials operating at high temperatures, ACS Nano 14 (7) (2020) 7696–7703.
- [4] Y. Liu, R. Zhang, J. Wang, Y. Wang, Current and future lithium-ion battery manufacturing, IScience 24 (4) (2021) 102332.
- [5] L. Lu, X. Han, J. Li, J. Hua, M. Ouyang, A review on the key issues for lithium-ion battery management in electric vehicles, J. Power Sources 226 (2013) 272–288.
- [6] J. Vetter, P. Novák, M. Wagner, C. Veit, K.-C. Möller, J. Besenhard, M. Winter, M. Wohlfahrt-Mehrens, C. Vogler, A. Hammouche, Ageing mechanisms in lithium-ion batteries, J. Power Sources 147 (1) (2005) 269–281.
- [7] M. Broussely, P. Biensan, F. Bonhomme, P. Blanchard, S. Herreyre, K. Nechev, R. Staniewicz, Main aging mechanisms in Li ion batteries, J. Power Sources 146 (1) (2005) 90–96.
- [8] J. Christensen, J. Newman, Cyclable lithium and capacity loss in Li-ion cells, J. Electrochem. Soc. 152 (4) (2005) A818.
- [9] U. Janakiraman, T.R. Garrick, M.E. Fortier, Review-lithium plating detection methods in Li-ion batteries, J. Electrochem. Soc. 167 (16) (2020) 160552.
- [10] Q. Liu, C. Du, B. Shen, P. Zuo, X. Cheng, Y. Ma, G. Yin, Y. Gao, Understanding undesirable anode lithium plating issues in lithium-ion batteries, RSC Adv. 6 (2016) 88683–88700.
- [11] A. Adam, J. Wandt, E. Knobbe, G. Bauer, A. Kwade, Fast-charging of automotive lithium-ion cells: In-situ lithium-plating detection and comparison of different cell designs, J. Electrochem. Soc. 167 (13) (2020) 130503.
- [12] X.-G. Yang, G. Zhang, S. Ge, C.-Y. Wang, Fast charging of lithium-ion batteries at all temperatures, Proc. Natl. Acad. Sci. 115 (28) (2018) 7266–7271.
- [13] J.C. Burns, D.A. Stevens, J.R. Dahn, In-situ detection of lithium plating using high precision coulometry, J. Electrochem. Soc. 162 (6) (2015) A959–A964.
- [14] M. Petzl, M.A. Danzer, Nondestructive detection, characterization, and quantification of lithium plating in commercial lithium-ion batteries, J. Power Sources 254 (2014) 80–87.
- [15] A. Jana, D.R. Ely, R.E. García, Dendrite-separator interactions in lithium-based batteries, J. Power Sources 275 (2015) 912–921.
- [16] G. Liu, W. Lu, A model of concurrent lithium dendrite growth, SEI growth, SEI penetration and regrowth. J. Electrochem. Soc. 164 (9) (2017) A1826–A1833.
- [17] C.T. Love, O.A. Baturina, K.E. Swider-Lyons, Observation of lithium dendrites at ambient temperature and below, ECS Electrochem. Lett. 4 (2) (2014) A24–A27.
- [18] T. Ohsaki, T. Kishi, T. Kuboki, N. Takami, N. Shimura, Y. Sato, M. Sekino, A. Satoh, Overcharge reaction of lithium-ion batteries, J. Power Sources 146 (1) (2005) 97-100
- [19] Y.C. Li, Y.S. Duh, J.M. Hsu, C.S. Kao, Thermal instability of organic esters and ethers with deposited lithium in lithium-ion battery, J. Therm. Anal. Calorim. 116 (3) (2014) 1219–1226.
- [20] S. Arrhenius, Über die dissociationswärme und den einfluss der temperatur auf den dissociationsgrad der elektrolyte, Z. Phys. Chem. 4U (1) (1889) 96–116.
- [21] T. Waldmann, B.-I. Hogg, M. Wohlfahrt-Mehrens, Li plating as unwanted side reaction in commercial Li-ion cells – A review, J. Power Sources 384 (2018) 107–124.
- [22] X. Lin, K. Khosravinia, X. Hu, J. Li, W. Lu, Lithium plating mechanism, detection, and mitigation in lithium-ion batteries, Prog. Energy Combust. Sci. 87 (2021) 100052
- [23] D. Ren, K. Smith, D. Guo, X. Han, X. Feng, L. Lu, M. Ouyang, J. Li, J. Electrochem. Soc. 165 (10) (2018) A2167–A2178.
- [24] X. Zhao, Y. Yin, Y. Hu, S.-Y. Choe, Electrochemical-thermal modeling of lithium plating/stripping of Li(Ni0.6Mn0.2Co0.2)O2/Carbon lithium-ion batteries at subzero ambient temperatures, J. Power Sources 418 (2019) 61–73.
- [25] T. Waldmann, B.-I. Hogg, M. Kasper, S. Grolleau, C.G. Couceiro, K. Trad, B.P. Matadi, M. Wohlfahrt-Mehrens, 2016, pp. A1232–A1238, 163 (7).
- [26] J. Cannarella, C.B. Arnold, Stress evolution and capacity fade in constrained lithium-ion pouch cells, J. Power Sources 245 (2014) 745–751.
- [27] J. Cannarella, C.B. Arnold, The effects of defects on localized plating in lithium-ion batteries, J. Electrochem. Soc. 162 (7) (2015) A1365–A1373.
- [28] C. Birkenmaier, B. Bitzer, M. Harzheim, A. Hintennach, T. Schleid, Lithium plating on graphite negative electrodes: Innovative qualitative and quantitative investigation methods, J. Electrochem. Soc. 162 (14) (2015) A2646–A2650.
- [29] J. Christensen, D. Cook, P. Albertus, An efficient parallelizable 3D thermoelectrochemical model of a Li-ion cell, 160 (11) (2013) A2258–A2267.

- [30] S.U. Kim, P. Albertus, D. Cook, C.W. Monroe, J. Christensen, Thermoelectrochemical simulations of performance and abuse in 50-Ah automotive cells, J. Power Sources 268 (2014) 625–633.
- [31] X. Zhang, M. Klinsmann, S. Chumakov, X. Li, S.U. Kim, M. Metzger, M.M. Besli, R. Klein, C. Linder, J. Christensen, A modified electrochemical model to account for mechanical effects due to lithium intercalation and external pressure, J. Electrochem. Soc. 168 (2) (2021) 020533.
- [32] X. Zhang, S. Chumakov, X. Li, M. Klinsmann, S.U. Kim, C. Linder, J. Christensen, An electro-chemo-thermo-mechanical coupled three-dimensional computational framework for lithium-ion batteries, J. Electrochem. Soc. 167 (16) (2020) 160542
- [33] M. Doyle, T.F. Fuller, J. Newman, Modeling of galvanostatic charge and discharge of the lithium/polymer/insertion cell, J. Electrochem. Soc. 140 (6) (1993) 1526–1533.
- [34] T.F. Fuller, M. Doyle, J. Newman, Simulation and optimization of the dual lithium ion insertion cell, J. Electrochem. Soc. 141 (1) (1994) 1–10.
- [35] T.F. Fuller, M. Doyle, J. Newman, Relaxation phenomena in lithium-ion-insertion cells, J. Electrochem. Soc. 141 (4) (1994) 982–990.
- [36] B. Rieger, S. Schlueter, S. Erhard, J. Schmalz, G. Reinhart, A. Jossen, Multi-scale investigation of thickness changes in a commercial pouch type lithium-ion battery, J. Energy Storage 6 (2016) 213–221.
- [37] J.H. Lee, H.M. Lee, S. Ahn, Battery dimensional changes occurring during charge/discharge cycles—thin rectangular lithium ion and polymer cells, J. Power Sources 119–121 (2003) 833–837.
- [38] D.A.G. Bruggeman, Berechnung verschiedener physikalischer konstanten von heterogenen substanzen. I. Dielektrizitätskonstanten und leitfähigkeiten der Mischkörper aus isotropen substanzen, Ann. Phys. 416 (7) (1935) 636–664.
- [39] H. Noh, S. Youn, C. Yoon, Y. Sun, Comparison of the structural and electrochemical properties of layered Li[Ni_xCo_yMn_z]O₂ (x=1/3, 0.5, 0.6, 0.7, 0.8 and 0.85) cathode material for lithium-ion batteries, J. Power Sources 233 (2013) 121–130.
- [40] J. Li, L.E. Downie, L. Ma, W. Qiu, J.R. Dahn, Study of the failure mechanisms of LiNi_{0.8}Mn_{0.1}Co_{0.1}O₂ cathode material for lithium ion batteries, 162 (7) (2015) A1401–A1408
- [41] K. Märker, P.J. Reeves, C. Xu, K.J. Griffith, C.P. Grey, Evolution of structure and lithium dynamics in LiNi0.8Mn0.1Co0.1o2 (NMC811) cathodes during electrochemical cycling, Chem. Mater. 31 (7) (2019) 2545–2554.
- [42] H. Sun, K. Zhao, Electronic structure and comparative properties of LiNixMnyCozO2 cathode materials, J. Phys. Chem. C 121 (11) (2017) 6002–6010.
- [43] J.A. Turner, S. Allu, S. Gorti, S. Kalnaus, A. Kumar, D. Lebrun-Grandie, S. Pannala, S. Simunovic, S. Stuart, H. Wang, Crash Models for Advanced Automotive Batteries, Technical Report, Oak Ridge National Laboratory, 2015.
- [44] I.V. Thorat, D.E. Stephenson, N.A. Zacharias, K. Zaghib, J.N. Harb, D.R. Wheeler, Quantifying tortuosity in porous Li-ion battery materials, J. Power Sources 188 (2) (2009) 592–600.
- [45] N. Zacharias, D. Nevers, C. Skelton, K. Knackstedt, D. Stephenson, D. Wheeler, Direct measurements of effective ionic transport in porous Li-ion electrodes, J. Electrochem. Soc. 160 (2012) A306–A311.
- [46] J. Landesfeind, H.A. Gasteiger, Temperature and concentration dependence of the ionic transport properties of lithium-ion battery electrolytes, J. Electrochem. Soc. 166 (14) (2019) A3079–A3097.
- [47] J. Landesfeind, J. Hattendorff, A. Ehrl, W.A. Wall, H.A. Gasteiger, Tortuosity determination of battery electrodes and separators by impedance spectroscopy, J. Electrochem. Soc. 163 (7) (2016) A1373–A1387.
- [48] L. Rao, J. Newman, Heat-generation rate and general energy balance for insertion battery systems, J. Electrochem. Soc. 144 (8) (1997) 2697–2704.
- [49] M.M. Besli, A. Subbaraman, F.R. Pour Safaei, C. Johnston, G. Schneider, N. Ravi, J. Christensen, Y. Liu, M.M. Doeff, M. Metzger, S. Kuppan, A study of model-based protective fast-charging and associated degradation in commercial smartphone cells: Insights on cathode degradation as a result of lithium depositions on the anode, Adv. Energy Mater. 11 (12) (2021) 2003019.
- [50] S. Zhang, K. Xu, T. Jow, The low temperature performance of Li-ion batteries, J. Power Sources 115 (1) (2003) 137–140.
- [51] A. Pesaran, S. Santhanagopalan, G.H. Kim, Addressing the impact of temperature extremes on large format Li-ion batteries for vehicle applications (Presentation), 2013, URL https://www.osti.gov/biblio/1082548.